



Ablation mechanism study on metallic materials with a 10 ps laser under high fluence

J. Cheng^{a,c,*}, W. Perrie^a, B. Wu^b, S. Tao^b, S.P. Edwardson^a, G. Dearden^a, K.G. Watkins^a

^a Laser Group, Department of Engineering, University of Liverpool, Brodie Building, Liverpool L69 3GQ, UK

^b Department of Mechanical, Materials and Aerospace Engineering, Illinois Institute of Technology, Chicago, IL 60616-3793, USA

^c Institute of Thermal Science and Technology, Shandong University, Shandong 250061, China

ARTICLE INFO

Article history:

Received 20 January 2009

Received in revised form 10 May 2009

Accepted 18 May 2009

Available online 22 May 2009

PACS:

52.38.Mf

52.50.Jm

Keywords:

Picosecond laser processing

Metals and alloys

Modeling of laser ablation

ABSTRACT

Single shot ablation of metallic materials of aluminium, titanium alloy (Ti6Al4V) and gold has been studied with 10 picoseconds (ps) laser pulses experimentally and theoretically. The ablation rate variation at high fluence was explained by a simplified predictive model based on critical-point phase separation (CPPS) theory. A comparison between experimental and numerical results inferred that CPPS may well be the dominant ablation mechanism for high fluence laser ablation at 10 ps laser duration.

Crown Copyright © 2009 Published by Elsevier B.V. All rights reserved.

1. Introduction

Femtosecond laser material processing has been widely studied from basic research to potential industrial applications [1–4]. Ultrafast laser pulses show advantages for material processing quality over long laser pulses because of the so-called “cold ablation” with minimum melt. However, when the laser fluence is increased well above ablation threshold, the advantages of ultrashort pulse processing are lost resulting in significant melting observed experimentally and predicted by simulation [5,6]. Moreover, femtosecond lasers show some shortcomings for industrial applications: the complexity of Chirped Pulse Amplification (CPA) leads to high cost, while kHz repetition rates result in low throughput via the need to attenuate to fluences $<1 \text{ J/cm}^2$. Recently, Dausinger pointed out that close to the ablation threshold, melt thickness with ultrashort pulses shows very little change for temporal pulse length up to 10 ps, while the nonlinear effects typically observed with femtosecond laser pulses are absent; hence precision micro-machining can be achieved with laser pulse lengths of 5–10 ps [7]. In fact, for most metals, the

electron–phonon coupling time is about several to tens of picoseconds, essentially the same temporal regime. Le Harzic et al. recently studied ablation of metals with pulse lengths from 100 fs to 5 ps and concluded that the effect of pulse length can be understood in terms of the thermal characteristics of metals such as electron–phonon coupling constants [8]. However, a complete understanding of the mechanism of picosecond ablation of materials is still required. Presently, picosecond laser systems with pulse lengths of around 10 ps and high repetition rate, up to 200 kHz, are commercially available, addressing the drawbacks mentioned above and hence the motivation for this work in terms of potential industrial applications.

Previous work has demonstrated that two ablation regimes exist for 10 ps pulse duration as with femtosecond (fs) pulse duration for aluminium, titanium alloy (Ti6Al4V) and gold, which have widely varying electron–phonon coupling times, and a qualitative two-temperature model analysis has been provided to explain ablation threshold under low fluence [9]. In this paper, follow-up work has been carried out to examine the ablation mechanism under high fluence by using a simplified predictive model based on critical-point phase separation (CPPS) theory. A comparison of measured ablation depths with those predicted by this model is shown. Single shot ablation allows one to investigate the ablation mechanism without the complication of multi-pulse incubation effects.

* Corresponding author at: Tel.: +44 1516502305; fax: +44 1516502304.

E-mail address: Jian.Cheng@liv.ac.uk (J. Cheng).

2. Experimental

The laser and experimental set-up have been described previously [9]. Briefly, the laser output beam traversed a $3\times$ beam expander and was then directed to a scanning galvanometer with a $f = 100$ mm f-theta lens (Nutfield). Focused spot size was observed to be 22 ± 0.2 μm in accordance with a Gaussian distribution at 1064 nm wavelength, almost diffraction limited. Samples were mounted on a 5-axis Aerotech precision motion control system running under NView MMI, which has a repeatability of 0.5 μm . The pulse energy was varied in the range of 0.2–50 μJ , corresponding to a peak fluence range of 0.08–25 J/cm^2 . Samples of aluminium (99%) and titanium alloy (Ti6Al4V Grade 5) were first mechanically polished and then ground with SiC grinding paper (400–1200 grit) down to a surface roughness (R_a) of ~ 20 nm, while the gold sample (99.9%) was a commercial gold coated copper mirror with almost a similar surface roughness (thickness of gold layer is 500–600 nm). As aluminium is the most chemically active, one expects that a 30–50 \AA thick Al_2O_3 layer is formed on the surface. However, this oxide layer is highly transparent and so thin that reflectivity and ablation behaviour will be essentially unaltered [10]. A series of holes were drilled with single pulses in order to study ablation without the complication of the incubation effect and hence simplifying theoretical modeling. Before and after laser ablation, all the samples were ultrasonically cleaned in methanol to remove the contamination and ablated debris. Microstructures were observed with a Nikon optical microscope with CCD camera and residual surface roughness, features and ablation depths determined by using a WYKO NT1100 optical surface profiling system.

3. Theory and modeling

3.1. Original model

During ultrafast laser micro-structuring of metals, theoretical models have been proposed based on hydrodynamics [11,12] and molecular dynamics [13–16]. For example, Nedialkov argued that thermal-elastic wave is the dominant mechanism for material removal just above the ablation threshold and then followed by phase explosion with increasing laser fluence [16]. Vidal [11] and Cheng [13] suggested that critical-point phase separation (CPPS) is the dominant mechanism for fs laser ablation under high fluence ($>$ several J/cm^2 or higher for most metals). For this theory, it is argued that for ultrashort laser ablation, the sample material cells near the surface will first be heated to their maximum temperature without obvious density change and then their temperature T and density ρ will decrease following roughly the expansion trajectories of $T \propto \rho^{2/3}$ (see the route of $O \rightarrow A \rightarrow CP$ in Fig. 1). It is also argued that the expansion trajectory of certain material cells will enter the thermodynamically unstable zone near the critical point, then these cells will transform into a bubble–droplet transition layer as a result of instabilities. The mass above these material cells will be ablated, while the mass below will condense back to the target. The maximum temperature of the material cells separating the ablated and un-ablated material, the separation temperature T_{sep} in this paper, is related to the thermodynamic critical temperature as follows:

$$\frac{T_{sep}}{T_c} = \left(\frac{\rho_0}{\rho_c} \right)^{2/3} \quad (1)$$

where T_c and ρ_c are the material critical temperature and density, respectively while ρ_0 is the material density at room temperature.

Following this analysis, by solving for the lattice temperature, the location beneath the surface where the maximum temperature

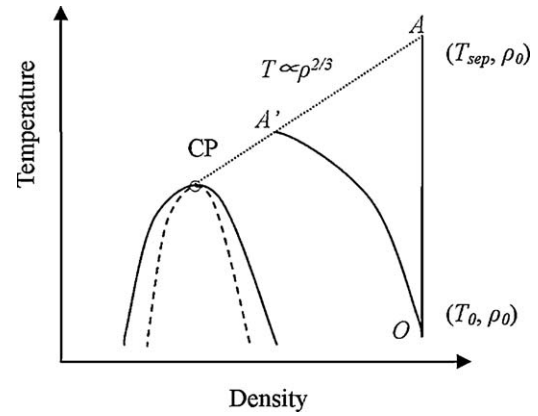


Fig. 1. A schematic diagram of the thermodynamic trajectory of the material based on CPPS theory. The dome in solid line is the binode. The dome in dashed line is the spinode. CP is the critical point.

is equal to the separation temperature can be calculated and then this location can be regarded approximately as the ablation depth. In order to get the lattice temperature, a one-dimensional, two-temperature model (TTM) [17] was used:

$$C_e(T_e) \frac{\partial T_e}{\partial t} = \frac{\partial}{\partial z} \left(\kappa \frac{\partial T_e}{\partial z} \right) - g(T_e - T_l) + S(z, t) \quad (2a)$$

$$C_l(T_l) \frac{\partial T_l}{\partial t} = g(T_e - T_l) \quad (2b)$$

where t is time, z is the spatial coordinate, T_e and T_l are electron and lattice temperatures, respectively; C_e and C_l are the electronic and lattice heat capacities, respectively; κ is the electron thermal conductivity; g is electron–phonon coupling constant and $S(z, t)$ represents the heating source from the laser pulse. The diffusive term is absent in the second equation because heat diffusion occurs much more rapidly through the electron gas than through lattice phonons.

C_e and C_l can be calculated from the quotidian equation of state (QEOS) model [18] at the normal density of metals. In the model, the data of electronic and lattice heat capacities are firstly obtained using the QEOS model, which has been widely used in the literature by numerous researchers (e.g., Refs. [11,19,20]). After that, the simulation has also been performed by incorporating the data on electron heat capacity and electron–phonon coupling taken from Ref. [21], where the data is obtained based on first-principles electronic structure calculations of the electron density of states. The simulation results based on QEOS and those obtained by incorporating the data from Ref. [21] will be compared.

κ can be obtained by using the model of Lee and More [22,23]. $g = C_e/\tau_e$ [19], where τ_e is the mean energy exchange time for electrons and lattice. The laser source term:

$$S(z, t) = -\frac{\partial I(z, t)}{\partial z} \quad (3a)$$

represents the actual absorbed laser energy by the sample, where $I(z, t)$ is the laser beam intensity at z , and can be obtained by solving the following equation:

$$\frac{\partial I(z, t)}{\partial z} = -\alpha I(z, t) \quad (3b)$$

where α is the absorption coefficient. At the sample surface ($z = 0$), $I(0, t) = (1 - R)I_0(t)$, where $I_0(t)$ is the intensity of the incoming laser beam on the sample surface, and R is the surface reflectivity. Based on the model of Lee and More [22], the dc conductivity can be

obtained, and then the values of α and R can be calculated according to Drude theory [11,24] and Fresnel formulas [25]:

$$\nu = \frac{n_e e^2}{m' \sigma_0} \quad (4)$$

$$w_p = \sqrt{\frac{n_e e^2}{m' \epsilon_0}} \quad (5)$$

$$n_r^2 - n_i^2 = 1 - \frac{w_p^2}{w^2 + \nu^2} \quad (6)$$

$$2n_r n_i = \frac{\nu w_p^2}{w(w^2 + \nu^2)} \quad (7)$$

$$\alpha = 2 \frac{w n_i}{c} \quad (8)$$

$$R = \frac{(n_r - 1)^2 + n_i^2}{(n_r + 1)^2 + n_i^2} \quad (9)$$

where w_p is the plasma frequency, ν is the electron collision frequency, σ_0 is the dc conductivity, ϵ_0 is the permittivity of vacuum, n_e is the electron number density, e is the electron charge, m' is the mass of the electron, n_r and n_i are the real and imaginary parts of the complex index of refraction, respectively w is the laser frequency, c is the speed of light and α is the aforementioned absorption coefficient.

Eqs. (2a) and (2b) can be solved by using a finite volume method, and then the temperature history at each material cell can be obtained. The initial location of the material cell whose maximum temperature is equal to the separation temperature can be taken approximately as the ablation depth. The separation temperature can be calculated using Eq. (1) based on the material critical temperature and density taken from Refs. [26–28]. This model has been verified in prior work for the fs laser ablation of aluminium and copper and has been found to be applicable for up to 10 ps laser ablation of copper [29]. It also should be mentioned here that this model is only valid for high fluence (>several J/cm² for most metals). When laser fluence is low, the ablation mechanism may not be critical-point phase separation.

3.2. Improved model

Even though the original model has been verified for fs laser ablation study of metals, it may not be very accurate for the 10 ps laser pulse. The laser pulse duration effect can be inferred from Eq. (1). In Eq. (1), the separation temperature, T_{sep} , is calculated with a state of the normal density and room temperature (T_0, ρ_0), which is very suitable for the fs laser pulse since under such condition, material will roughly follow the route of $O \rightarrow A \rightarrow CP$ (Fig. 1) and then come into the unstable zone. However, for 10 ps laser ablation, this much longer laser pulse may give some time for material expansion and density decrease. Hence the separation temperature, T_{sep} , will drop because of a density decrease from ρ_0 to a smaller value and then material may follow the route of $O \rightarrow A' \rightarrow CP$ (Fig. 1). That is, the actual separation temperature (the temperature of A') may be lower than the one calculated using Eq. (1) (the temperature of A), and hence the model may underestimate the ablation depth. It should be noted that Fig. 1 is just a rough schematic not drawn to the actual scale, and more detailed theoretical study is required to get more exact thermodynamic trajectories of materials.

Following the above analysis, the model can be improved by using the temperature of point A' as the effective separation temperature instead of using the temperature of point A . Then, the ablation depth will be the initial depth of the location where the maximum temperature is equal to the effective separation temperature.

If the density of point A' , $\rho_{A'}$, is known, then the temperature of the point A' , $T_{A'}$, can be calculated as:

$$\frac{T_{A'}}{T_c} = \left(\frac{\rho_{A'}}{\rho_c} \right)^{2/3} \quad (10)$$

where T_c and ρ_c are the critical temperature and density, respectively. Then $T_{A'}$ can be used as the separation temperature in the model, that is: $T_{sep} = T_{A'}$.

The next question is how to obtain the density of A' . Strictly speaking, this requires molecular dynamics simulation or full hydrodynamic simulations supplemented by a wide-range equation of state, which will be very complicated and computationally expensive (it is certainly a good work in the future). This, however, will contradict the purpose of the simplified model in the paper, which is to predict the ablation depth with very small computational cost and without involving any free adjustable variables.

The hydrodynamic simulation in Ref. [11] implies that as metals are driven by high-intensity short laser pulses to a very high temperature and pressure, their expansion behaviours may be roughly similar to ideal gas. Because the ambient air pressure is negligible compared with the laser-induced high pressure in metals, the laser-induced metal expansion process can be very roughly analyzed as a process of unsteady ideal gas flow into a vacuum.

The analytical solution to the well-known problem of one-dimensional unsteady gas flow into a vacuum is given in Ref. [30]. For uniform ideal gas initially occupying the $z \leq 0$ region with density of ρ_0 , as it starts expanding (at $t = 0$) into the vacuum in the $z > 0$ region, the gas surface will move in the $+z$ direction with a velocity of $(2/\gamma - 1)c_0$, where c_0 is the sound speed and γ is the isentropic exponent. Hence the surface location at t will be $z = (2/\gamma - 1)c_0 t$. Due to the expansion, the gas density will decrease and hence a rarefaction wave will propagate in the $-z$ direction at the sound speed c_0 . Therefore, the rarefaction wave front at t is $z = -c_0 t$. The gas velocity u is 0 for $z \leq -c_0 t$. From $z = -c_0 t$ to the surface location $z = (2/\gamma - 1)c_0 t$, the velocity increases linearly (with respect to z) to the maximum value of $(2/\gamma - 1)c_0$ at the surface. From the above, for any given time, the gas velocity is given by:

$$u = \begin{cases} \frac{2}{\gamma + 1} \left(c_0 + \frac{z}{t} \right) & \text{for } -c_0 t \leq z \leq \frac{2}{\gamma - 1} c_0 t \\ 0 & \text{for } z < -c_0 t \end{cases} \quad (11)$$

Then the density can be calculated as:

$$\rho = \rho_0 \left[1 - \frac{\gamma - 1}{2} \frac{|u|}{c_0} \right]^{2/(\gamma - 1)} \quad (12)$$

Using the above approach, the density of the separation point can be roughly estimated. Then the effective separation temperature can be calculated using Eq. (10). Again, it should be noted that the above approach, although it certainly has relevant physical meaning, can only provide a rough estimation. A more strict calculation requires molecular dynamics simulation or full hydrodynamic simulation supplemented by a wide-range equation of state for the metals.

The major material properties used in the model have been summarized in Table 1. Note that for the improved model, the electronic heat capacities, C_e , are calculated from QEOS. Electron-phonon coupling constants, g , are calculated as $g = C_e/\tau_e$ (where C_e is from QEOS).

4. Results and discussions

In this work, the experimental ablation depths were measured by averaging over five drilled holes at each fluence. In Figs. 2–4, the squared dots and circled lines present the experimental and

Table 1
Summary of the major material properties used in the model.

Material properties used in the model	Values or sources
The electronic capacities, C_e	Calculated using the QEOS model [18] or taken from Ref. [21]
The lattice heat capacities, C_l	Calculated using QEOS model [18]
The electron thermal conductivity, κ	Calculated using the model of Lee and More [22].
Optical index of refraction and absorption coefficient	Calculated using the Drude model (based on the dc conductivity calculated using the model of Lee and More [22])
The mean energy exchange time for electrons and lattice, τ_e	Aluminium: 4 ps; titanium: 7 ps; gold: 119 ps [8,31].
Electron–phonon coupling constant, g	Calculated as $g = C_e/\tau_e$ (where C_e is from QEOS) or taken from Ref. [21].
Material critical temperature, T_c	Aluminium: 5410 K; titanium: 7500 K; gold: 7400 K [26–28].
Material critical density, ρ_c	Titanium: 1009 kg/m ³ ; aluminium: 490 kg/m ³ ; gold: 7.69×10^3 kg/m ³ [26–28].

simulation results of ablation rate (based on QEOS) versus laser fluence for the three aforementioned metals. In Fig. 2, the simulation results for aluminium cover the laser fluence range of 2–25 J/cm², which is the electron heat diffusion governed regime. For the simulation results, the simulated ablation rate increases from 25 nm per pulse at 2 J/cm² to 308 nm per pulse at 16 J/cm² while the experimental ablation rates are approximately 150 nm per pulse and 600 nm per pulse at these fluences. While the trend in ablation rate is predicted, the experimental ablation rates are several times higher than the modeling predictions, converging only at fluence >15 J/cm². In Fig. 3, somewhat better agreement between experiment and simulation is observed for the titanium alloy; however, the simulation underestimates ablation rate generally by a factor of 2 below fluence at ~10 J/cm². The simulated ablation rates of 24 and 205 nm per pulse at 2 and 16 J/cm², respectively correspond to the experimental data of approximately 80 and 200 nm per pulse. For gold, modeling results (based on QEOS) show that the peak temperature does not reach the separation temperature when laser fluence is below 5 J/cm². Thus, in Fig. 4, the ablation rate comparison is shown for laser fluence from 6 J/cm² to 20 J/cm².

The simulation has also been performed by incorporating the data on electron heat capacity and electron–phonon coupling taken from Ref. [21]. The results have also been shown in Figs. 2–4 (triangled lines). It can be seen that for aluminium, the simulation

results based on QEOS and those incorporating the data from Ref. [21] are very close. For Ti6Al4V and gold, the differences become more obvious. The agreements between simulations and measurements have not been improved by incorporating the data on electron heat capacity and electron–phonon coupling taken from Ref. [21].

In Figs. 2–4, the starred lines show the simulation results using the separation temperature calculated with Eq. (10). It can be seen that agreements between simulations and experimental measurements have been significantly improved compared to the results obtained based on QEOS and the data from Ref. [21]. Considering the simulations are performed with a simplified model with very small computational cost and without any free adjustable variables, the agreements between simulations and measurements are reasonably good. The good agreements have shown that the simple approach (Eq. (11)) used in the model to estimate the density decrease due to expansion, although very rough, can still provide physically meaningful estimation.

In this study, the three metals selected have a wide variation in electron–phonon coupling times. Aluminium has the shortest electron–phonon coupling time of about 4 ps, compared with titanium of 7 ps and gold of over 100 ps [8,31]. The modeling predictions based on the CPPS theory have shown reasonably good agreements with the experimental results for all the three metals,

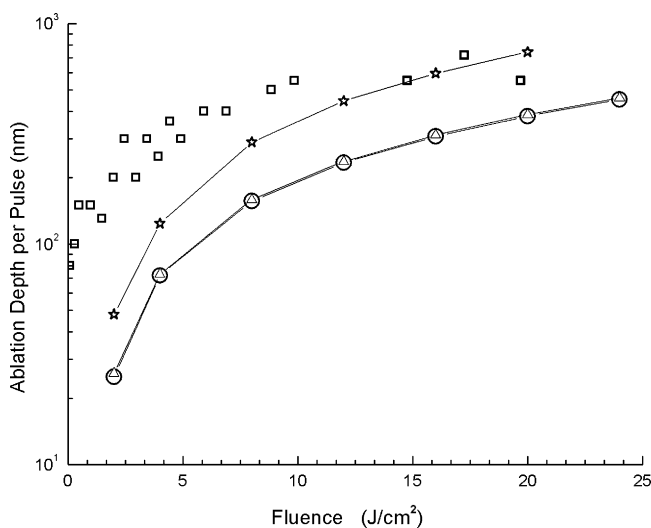


Fig. 2. The experimental and theoretical comparison of ablation rate for aluminium with laser fluence. The squared dots present the experimental data; the circled line presents the simulation results based on QEOS; the triangled line presents the simulation results by incorporating the data on electron heat capacity and electron–phonon coupling taken from Ref. [21]; the starred line presents the simulation results by the improved model with the data of electron heat capacity and electron–phonon coupling from QEOS.

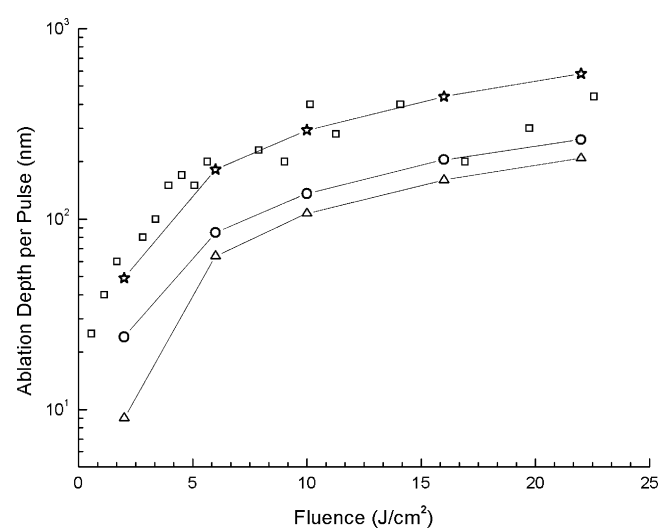


Fig. 3. The experimental and theoretical comparison of ablation rate for Ti6Al4V with laser fluence. The squared dots present the experimental data; the circled line presents the simulation results based on QEOS; the triangled line presents the simulation results by incorporating the data on electron heat capacity and electron–phonon coupling taken from Ref. [21]; the starred line presents the simulation results by the improved model with the data of electron heat capacity and electron–phonon coupling from QEOS.

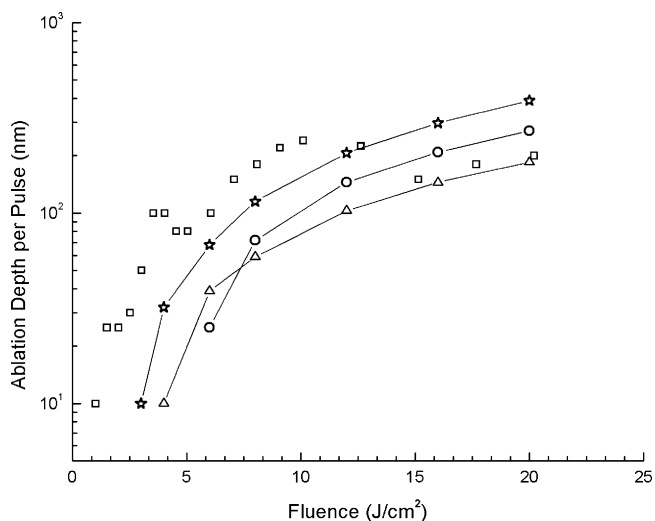


Fig. 4. The experimental and theoretical comparison of ablation rate for gold with laser fluence. The squared dots present the experimental data; the circled line presents the simulation results based on QEOS; the triangled line presents the simulation results by incorporating the data on electron heat capacity and electron-phonon coupling taken from Ref. [21]; the starred line presents the simulation results by the improved model with the data of electron heat capacity and electron-phonon coupling from QEOS.

which indicate that the critical-point phase separation could be the relevant dominant ablation mechanism for the high fluence laser ablation studied here.

5. Conclusions

Single shot 10 ps laser ablation on aluminium, titanium alloy and gold at a wavelength of 1064 nm was studied experimentally and theoretically. Simulations have been performed using a simplified predictive model based on the “separation temperature” concept and the critical-point phase separation mechanism. If the possible target material density decrease due to laser-induced expansion is considered during the calculation of the separation temperature, reasonably good agreement can be obtained between experimental data and modeling predictions, which shows that critical-point phase separation could be the relevant ablation mechanism for high laser fluence. Due to the complicated physics involved in picosecond laser ablation, more detailed experimental and theoretical work is still needed to further clarify the ablation mechanism.

Acknowledgements

The authors gratefully acknowledge the support of the North West Development Agency (NWDA) in the UK. J. Cheng would like to thank UK/China Postgraduate Research Scholarships for Excellence and the China Scholarship Council for their financial support.

References

- [1] P.P. Ponko, S.K. Dutta, J. Squier, J.V. Rudd, D. Du, G. Mourou, *Opt. Commun.* 114 (1995) 106.
- [2] B.N. Chichkov, C. Momma, S. Nolte, F. von Alvensleben, A. Tünnermann, *Appl. Phys. A* 63 (1996) 109.
- [3] P. Simon, J. Ihlemann, *Appl. Phys. A* 63 (1996) 505.
- [4] W. Perrie, A. Rushton, M. Gill, P. Fox, W. O’Neill, *Appl. Surf. Sci.* 248 (2005) 213.
- [5] S.I. Kudryashov, *Proc. SPIE* 6106 (2006) 61061C.
- [6] J.P. Colombier, P. Combis, R. Stoian, E. Audouard, *Phys. Rev. B* 75 (2007) 104105.
- [7] F. Dausinger, *Proc. SPIE* 5777 (2005) 840.
- [8] R. Le Harzic, D. Breitling, M. Weikert, S. Sommer, C. Föhl, S. Valette, C. Donnet, E. Audouard, F. Dausinger, *Appl. Surf. Sci.* 249 (2005) 322.
- [9] J. Cheng, W. Perrie, M. Sharp, S.P. Edwardson, N.G. Semaltianos, G. Dearden, K.G. Watkins, *Appl. Phys. A* 95 (2009) 739.
- [10] F. Amman, G.P. Banfi, P.G. Gobbi, S. Morosi, G.C. Reali, *Plasma Phys.* 22 (1980) 453.
- [11] F. Vidal, T.W. Johnston, S. Laville, O. Barthelemy, M. Chaker, B.L. Drogoff, J. Margot, M. Sabsabi, *Phys. Rev. Lett.* 86 (2001) 2573.
- [12] J.P. Colombier, P. Combis, F. Bonneau, R. Le Harzic, E. Audouard, *Phys. Rev. B* 71 (2005) 165406.
- [13] C. Cheng, X. Xu, *Phys. Rev. B* 72 (2005) 165415.
- [14] S.E. Imamova, P.A. Atanasov, N.N. Nedialkov, F. Dausinger, P. Berger, *Nucl. Instrum. Meth. Phys. Res. B* 227 (2005) 490.
- [15] N.N. Nedialkov, S.E. Imamova, P.A. Atanasov, P. Berger, F. Dausinger, *Appl. Surf. Sci.* 247 (2005) 243.
- [16] N.N. Nedialkov, P.A. Atanasov, S. Amoruso, R. Bruzzese, X. Wang, *Appl. Surf. Sci.* 253 (2007) 7761.
- [17] S.I. Anisimov, B. Kapeliovich, T.L. Perel’man, *Sov. Phys. JETP* 39 (1974) 375.
- [18] R.M. More, K.H. Warren, D.A. Young, G.B. Zimmerman, *Phys. Fluids* 31 (1988) 3059.
- [19] S. Laville, F. Vidal, T.W. Johnston, O. Barthelemy, M. Chaker, B.L. Drogoff, J. Margot, M. Sabsabi, *Phys. Rev. E* 66 (2002) 066415.
- [20] A. Ng, A. Forsman, G. Chiu, *Phys. Rev. Lett.* 81 (1998) 29.
- [21] Z. Lin, L.V. Zhigilei, V. Celli, *Phys. Rev. B* 77 (2008) 075133.
- [22] Y.T. Lee, R.M. More, *Phys. Fluids* 27 (1984) 1273.
- [23] M.P. Desjarlais, *Contrib. Plasma Phys.* 41 (2001) 267.
- [24] F.L. Pedrotti, L.S. Pedrotti, *Introduction to Optics*, Englewood Cliffs/Prentice Hall, Upper Saddle River, NJ, USA, 1993.
- [25] J.F. Ready, *LIA Handbook of Laser Material Processing*, Magnolia Publishing Inc., 2001.
- [26] M.M. Martynyuk, *Russ. J. Phys. Chem.* 57 (1983) 494.
- [27] K. Boboridis, G. Pottlacher, H. Jager, *Int. J. Thermophys.* 20 (1999) 1289.
- [28] M. Hoch, *J. Nucl. Mater.* 152 (1988) 289.
- [29] B. Wu, Y.C. Shin, *Appl. Surf. Sci.* 253 (2007) 4079.
- [30] Y.B. Zel’dovich, P.R. Raizer, *Physics of Shock Waves and High Temperature Hydrodynamic Phenomena*, Academic Press, New York/London, 1966.
- [31] S.D. Broson, A. Kazeroonian, J.S. Moodera, D.W. Face, T.K. Cheng, E.P. Ippen, M.S. Dresselhaus, G. Dresselhaus, *Phys. Rev. Lett.* 64 (1990) 2172.